Spectroscopic and transport studies of Co_xFe_{1-x}/MgO(001)-based magnetic tunnel junctions

S. Andrieu,[1,*] L. Calmels,[2] T. Hauet,[1] F. Bonell,[1,†] P. Le Fèvre,[3] and F. Bertran[3]

[1]*Institut Jean Lamour, Université de Lorraine/CNRS, Boulevard des Aiguillettes, B.P. 239, 54506 Vandœuvre-lès-Nancy, France*

[2]*CEMES, CNRS, and Université de Toulouse, 29 rue Jeanne Marvig, B.P. 94347, 31055 Toulouse Cedex 4, France*

[3]*Synchrotron SOLEIL-CNRS, L'Orme des Merisiers, Saint-Aubin, B.P. 48, 91192 Gif-sur-Yvette Cedex, France*

(Received 26 June 2014; revised manuscript received 5 November 2014; published 1 December 2014)

$Fe_{1-x}Co_x$ epitaxial layers were grown by molecular beam epitaxy and controlled using *in situ* characterization tools (electron diffraction, x-ray photoelectron, and Auger spectroscopies) in order to use these alloys in magnetic tunnel junctions. Thick films are shown to be BCC up to $x = 70\%$, whereas thin films grown on Fe(001) are BCC over the whole Co concentration range up to a critical thickness. Fe/Co intermixing is also examined in detail. The tunnel magnetoresistance and conductance of MgO-based magnetic tunnel junctions built with BCC $Fe_{1-x}Co_x$ electrodes show peculiar voltage dependencies. Their interpretation relies on spin- and symmetry-resolved photoemission measurements and *ab initio* calculations. The bulk and interfacial occupied states detected by photoemission are compared to the calculated ones. Experimental results and *ab initio* calculations are in good agreement. Finally, the experimental conductance curves are compared to the autoconvolution of the $\Delta 1$ density of states in which both bulk and interface states are taken into account.

DOI: 10.1103/PhysRevB.90.214406 PACS number(s): 72.25.−b, 73.40.Gk, 81.15.Hi

I. INTRODUCTION

In 2001, a huge tunnel magnetoresistance (TMR) was theoretically predicted in the single-crystalline Fe/MgO/Fe(001) system. The spin-polarized transport in fully epitaxial MgO-based magnetic tunnel junctions (MTJs) is explained by considering the full spin polarization of states with $\Delta 1$ symmetry in Fe and the symmetry filtering of the MgO barrier [1,2]. TMR values as large as 1000% in Fe/MgO/Fe(001) and several thousands percent in FeCo/MgO/FeCo and BCC-Co/MgO/BCC-Co MTJs were calculated at 0 K [3]. This TMR increase when incorporating Co in Fe can be simply explained, as shown later in this paper. Actually, high TMR values have been experimentally measured in Fe/MgO- or FeCo(B)/MgO(001)-based MTJs by several groups since 2003 [4–6]. However, the observed TMR values are not as large as the predicted ones. Although the electronic properties at the Fe/MgO interface observed experimentally are in good agreement with theoretical predictions [7,8], some imperfections may partly explain this TMR discrepancy, like impurities at the interfaces [9–11] or defects in the barrier [12–14]. Nevertheless, the most contradictory and intriguing results were obtained with $Fe_{1-x}Co_x$/MgO(001)-based MTJs [3,15–18]. These discrepancies are observed, on the one hand, between experimental results and calculations and, on the other hand, between different experimental results reported in the literature.

The reported results are the following.

(i) The calculations were performed in the case of an equimolar and B2-ordered $Fe_{0.5}Co_{0.5}$ alloy and for pure BCC Co. The main trend is that increasing the Co concentration should result in larger experimental TMR values [3].

(ii) The large reported TMR value on molecular beam epitaxy (MBE)–grown Fe/BCC-Co/MgO/Co/Fe(001)[16] seems to be in agreement with the calculations.

(iii) Epitaxial $Fe_{0.5}Co_{0.5}$/MgO/Fe(001) and Fe/MgO/Fe(001) MTJs exhibit the same TMR value [15,18], in contradiction to the calculations.

(iv) The reported TMR of sputtered $Fe_{1-x}Co_xB$/MgO/$Fe_{1-x}Co_xB$(001) MTJs presents a nonmonotonic dependence as a function of the Co content, with a maximum around 25% of Co [17]. This is, again, in contradiction to calculations but this was explained by a bad BCC-FeCo crystallization for a high Co content.

(v) A similar nonmonotonic dependence is observed in well-crystalized MBE-grown $Fe_{1-x}Co_x$/MgO/$Fe_{1-x}Co_x$ MTJs [18].

The situation was thus unclear. In this paper, first, we show that the assumption "a large Co content implies a large TMR" is actually wrong. Considering the whole Co concentration range, we show that *ab initio* calculations taking into account the chemical disorder lead to subtle electronic band structure modifications that do not appear in the previous calculations considering equimolar ordered FeCo alloys. Second, we show that Fe/Co intermixing occurs upon mild annealing, which probably accounts for the large TMR value observed in Ref. [16]. Moreover, additional spin- and symmetry-resolved photoemission results complete our previous work [18] and allow us to highlight the very good description of the "bulk" electronic band structure derived from *ab initio* calculations. The role of the interface state (IS) we evidenced by photoemission [18] was also considered in order to explain the peculiar behavior observed in conductance curves.

The paper is organized as follows. In Secs. II and III we present the sample growth analysis and tunnel junction preparation performed at the Institut Jean Lamour (IJL). As photoemission is a surface sensitive technique, dedicated samples were grown on the CASSIOPEE beamline at SOLEIL using the growth process established at IJL. The photoemission experiments are detailed in Sec. IV and compared to *ab initio*

*stephane.andrieu@univ-lorraine.fr

†Present address: Institut Català de Nanociència i Nanotecnologia, 08193 Bellaterra, Spain.

calculations described in Sec. V. A general discussion is also presented in Sec. V.

II. SAMPLE GROWTH DETAILS

The growth analysis was performed on samples grown by MBE at IJL. $Fe_{1-x}Co_x$ alloys were grown by coevaporation of Fe and Co sublimated from Knudsen cells in the range 1100–1250°C and 1300–1500°C, respectively. Epitaxy was checked using reflection high-energy electron diffraction (RHEED) during the growth of pure Fe, pure Co, or $Fe_{1-x}Co_x$ alloys on Fe(001) buffer layers. The alloy stoichiometry was controlled by measuring accurately the Fe and Co fluxes impinging on the substrate using two techniques. The first one was to measure the growth rates on a quartz microbalance at the sample location. The second, and more accurate one, consisted in recording RHEED intensity oscillations during the deposition of Co, Fe, or $Fe_{1-x}Co_x$. Indeed, if the growth is layer by layer, RHEED intensity oscillations are observed, the period of the oscillations corresponding to the time required to complete one atomic layer. Such experiments were performed on a Fe(001) buffer layer, the growth mode being actually layer by layer. To vary the Co content in $Fe_{1-x}Co_x$ alloys, the Co or Fe growth rate is varied by changing the Co or Fe flux (by changing the Fe or Co cell temperature). The true x content is thus determined by growing, first, pure Co (or Fe) and, second, FeCo in the same RHEED intensity oscillation run [Fig. 1(a)]. The relation between the fluxes ϕ (each flux being proportional to N, the atomic density of the growing atomic plane, divided by T, the time to complete a layer) thus leads to the equation

$$\phi_{\mathrm{FeCo}} = \phi_{\mathrm{Fe}} + \phi_{\mathrm{Co}} \rightarrow \frac{N_{\mathrm{FeCo}}}{T_{\mathrm{FeCo}}} = \frac{N_{\mathrm{Co}}}{T_{\mathrm{Co}}} + \frac{N_{\mathrm{Fe}}}{T_{\mathrm{Fe}}}. \quad (1)$$

Consequently, working at a fixed Co flux (fixed T_{Co}) leads to the linear equation

$$\frac{1}{T_{\mathrm{FeCo}}} = \frac{a}{T_{\mathrm{Fe}}} + b \quad \text{with} \quad a = \frac{N_{\mathrm{Fe}}}{N_{\mathrm{FeCo}}}$$
$$\text{and} \quad 1 - x = \frac{\phi_{\mathrm{Fe}}}{\phi_{\mathrm{FeCo}}} = \frac{1}{a}\frac{T_{\mathrm{FeCo}}}{T_{\mathrm{Fe}}}, \quad (2)$$

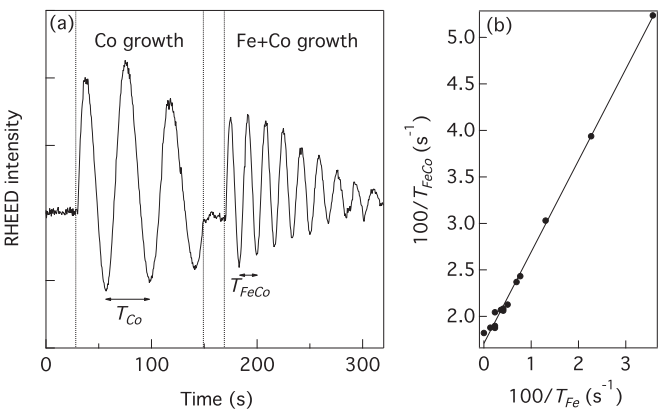

FIG. 1. (a) RHEED intensity oscillations during the growth of, first, Co alone and, second, a FeCo alloy on a Fe(001) buffer layer. (b) Working at a fixed Co growth rate and varying the Fe growth rate leads to a linear variation of the inverse of both periods as in Eq. (2).

while working at a fixed Fe flux leads to

$$\frac{1}{T_{\mathrm{FeCo}}} = \frac{c}{T_{\mathrm{Co}}} + d \quad \text{with} \quad c = \frac{N_{\mathrm{Co}}}{N_{\mathrm{FeCo}}}$$
$$\text{and} \quad x = \frac{\phi_{\mathrm{Co}}}{\phi_{\mathrm{FeCo}}} = \frac{1}{c}\frac{T_{\mathrm{FeCo}}}{T_{\mathrm{Co}}}. \quad (3)$$

This analysis was double-checked by doing a series of RHEED oscillation experiments (i) by fixing the Co flux and varying the Fe flux [Eq. (2)] or (ii) by fixing the Fe flux and varying the Co flux [Eq. (3)]. Results in case i are reported in Fig. 1(b). A linear relationship between $1/T_{\mathrm{FeCo}}$ and $1/T_{\mathrm{Fe}}$ is actually observed. A slope $a = 0.985 \pm 0.017$ is found, which means that the atomic densities are actually similar in BCC $Fe_{1-x}Co_x$ alloys and BCC Fe. This is consistent with pseudomorphic growth of $Fe_{1-x}Co_x$ on the Fe(001) surface. The Co content is simply the ratio of the oscillation periods of $Fe_{1-x}Co_x$ and Co in this case [Eq. (3)]. However, this control of the stoichiometry is not possible when growing the films directly on MgO as in MTJ preparation, because the growth of metals on MgO is usually not layer by layer. To control the Co content in this case, we performed x-ray photoemission spectroscopy (XPS; using an Al anode) at the Co and Fe $2p$ core levels [Fig. 2(a)]. We confirm that the peak ratio $I_{\mathrm{Fe}\,2p}/I_{\mathrm{Co}\,2p}$ is linearly dependent on $(1-x)/x$ as expected [19]. Our protocol was to determine the stoichiometry using RHEED during FeCo alloy growth on Fe(001) buffers and then to record the corresponding $I_{\mathrm{Fe}\,2p}/I_{\mathrm{Co}\,2p}$. The obtained $I_{\mathrm{Fe}\,2p}/I_{\mathrm{Co}\,2p}$ curve [Fig. 2(b)] was then used as a reference for any grown alloys.

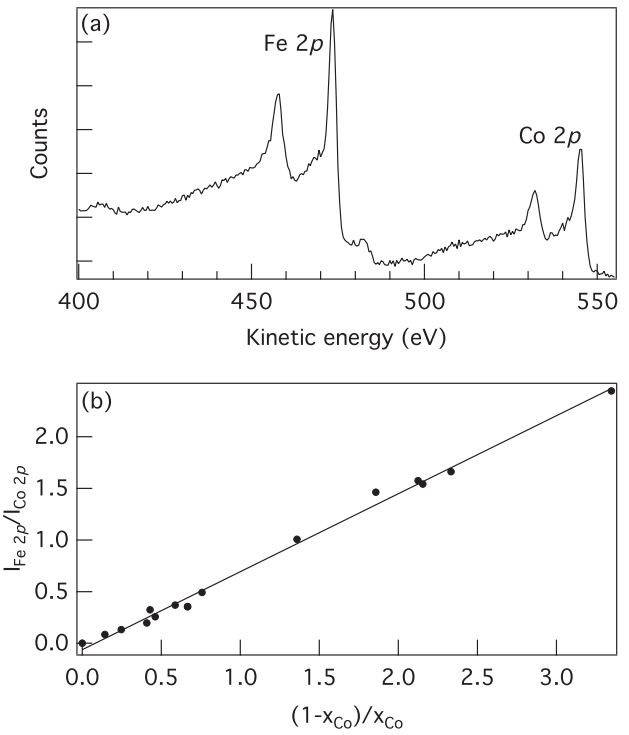

FIG. 2. (a) Example of XPS Fe $2p$ and Co $2p$ spectra obtained on a $Fe_{0.7}Co_{0.3}$ film and (b) variation of the $2p$ intensity ratio with the Fe and Co content ratio determined using RHEED for a series of $Fe_{1-x}Co_x$ films.

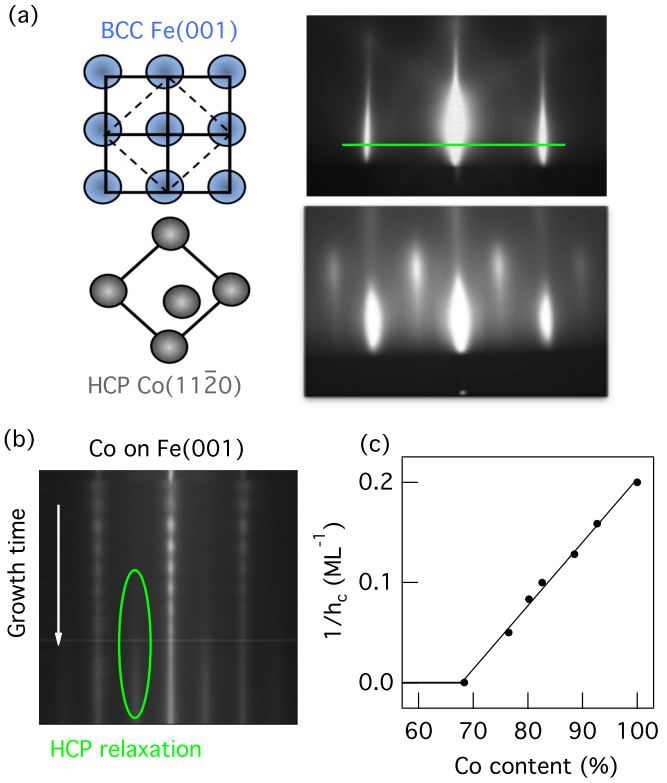

FIG. 3. (Color online) (a) Epitaxial relationship between HCP Co and Fe(001) and associated RHEED patterns along the [01] azimuth of the square Fe lattice. (b) RHEED intensity profile evolution during Co growth on Fe showing the HCP relaxation critical thickness (circle). (c) Deduced critical thickness dependence on the Co content.

Another key point to get large TMR values is to keep the BCC structure in $Fe_{1-x}Co_x$ layers. The crystalline structure of bulk $Fe_{1-x}Co_x$ layers is known to be BCC up to x around 70% and HCP for higher Co contents [20]. However, it is possible to stabilize the BCC structure for the whole Co concentration range by growing $Fe_{1-x}Co_x$ alloy thin films on a BCC Fe(001) buffer layer. At the beginning of the growth process, the $Fe_{1-x}Co_x$ alloys adopt the Fe(001) square lattice, and the RHEED patterns are unchanged. Above a critical thickness that depends on x, the $Fe_{1-x}Co_x$ alloy relaxation to HCP is detectable by RHEED since new streaks appear due to the special epitaxial relationship HCP(11$\bar{2}$0)//BCC(001) as shown in Fig. 3(a). The detection of these new streaks is consequently used to determine the critical thickness for relaxation, by recording a profile along streaks during deposition [Fig. 3(b)]. In this pattern, we also clearly observe the RHEED intensity oscillations that are used to convert the deposition time in atomic monolayers. The critical thickness h_c for plastic relaxation was determined in this way for the whole Co concentration range [Fig. 3(c)]. The linear variation between $1/h_c$ and x (linked to the misfit between Fe and the $Fe_{1-x}Co_x$ growing alloy) is consistent with the elastic model [21]. The critical thickness is only 5 monolayers (ML) for pure Co films and becomes infinite below 70% Co as expected since the BCC structure is the stable phase of these $Fe_{1-x}Co_x$ alloys.

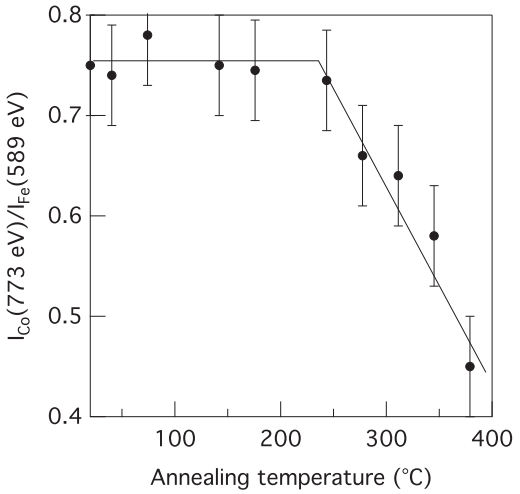

FIG. 4. Variation of the Co and Fe Auger peak ratio with annealing temperature for a 4-ML Co film deposited on a thick Fe layer. Intermixing starts at 250°C.

An important conclusion is that BCC $Fe_{1-x}Co_x$/MgO-based MTJs with x larger than 70% cannot be prepared with thick FeCo electrodes. However, for spin-resolved photoemission analysis, which is a surface technique (detecting depth of a few atomic planes), it is possible to get information for the whole x range by growing the alloys on Fe(001) buffers, limiting their thickness below the critical thickness of relaxation. Usually, an annealing is needed to improve the crystal quality and TMR [4–6,15–18]. The influence of annealing on the $Fe_{1-x}Co_x$/MgO interface is negligible because the intermixing between $Fe_{1-x}Co_x$ and MgO occurs only at very high temperatures (around 1200 K in our system). However, intermixing at the Fe/$Fe_{1-x}Co_x$ interface is expected to occur at much lower temperatures. We therefore checked the condition for intermixing between Co and Fe by using Auger electron spectroscopy (AES). A 4-ML Co film was grown on a Fe(001) buffer layer at room temperature and the Co-to-Fe intensity ratio was monitored using AES as a function of the annealing temperature. The temperature was raised in steps of 50 K and the AES spectra were measured just after temperature stabilization (which takes around 10 mn). The results are shown in Fig. 4. Intermixing is clearly observed above 250°C, as measured with a thermocouple located behind the sample holder. To avoid any intermixing problem in samples grown for photoemission analysis, the $Fe_{1-x}Co_x$ films grown on Fe(001) were never annealed. To complete our magnetotransport study, we also prepared Fe/BCC-Co (4 ML)/MgO/Co(4 ML)/Fe(001) MTJs, but without annealing. The TMR of these Co/MgO/Co MTJs measured at 20 K in four samples was around 90%, which is far below the 507% reported in Ref. [16]. The occurrence of Fe/Co intermixing at moderate temperatures probably explains this discrepancy since, in Ref. [16], an annealing at 250°C was performed during 30 min in order to optimize the TMR. According to our results on $Fe_{1-x}Co_x$/MgO/$Fe_{1-x}Co_x$ MTJs [18], their annealing process probably leads to an $Fe_{0.75}Co_{0.25}$ alloy.

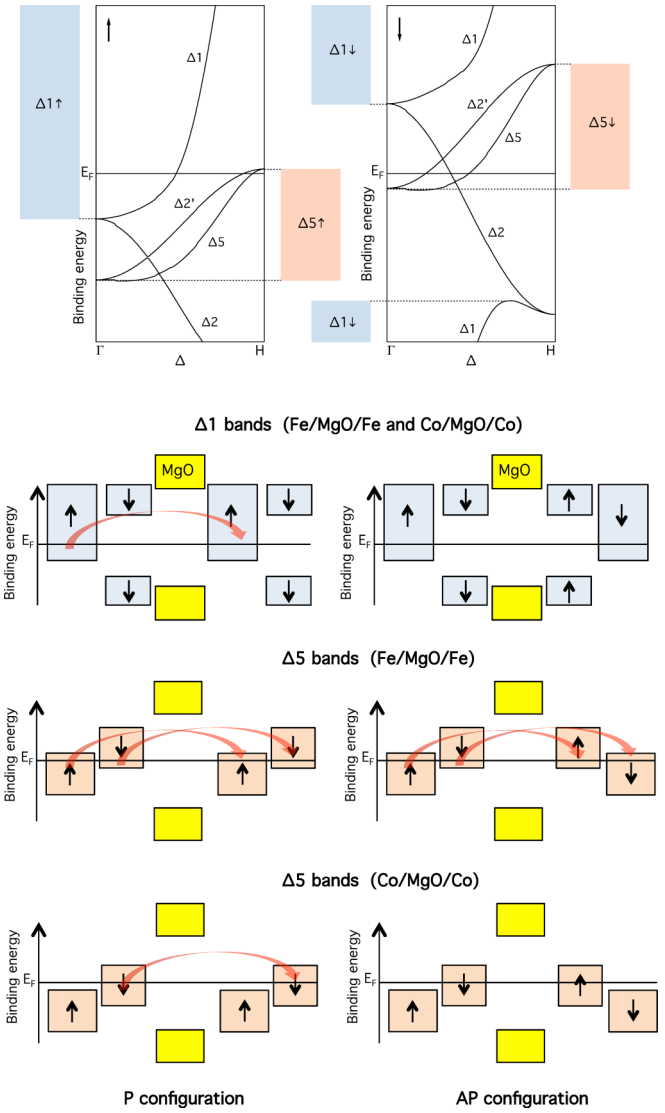

FIG. 5. (Color online) (Top) Schematic of the bands in the Fe BCC structure and (bottom) possible coherent tunneling channels when the magnetizations of both layers in the magnetic tunnel junctions are parallel (P) or antiparallel (AP). Up arrows, majority spin; down arrows, minority spin. Note that there is no more coherent tunneling in AP when considering Co instead of Fe. This simply explains why TMR values should be larger using Co instead of Fe.

III. MTJ PREPARATION AND TRANSPORT PROPERTIES

To understand easily why the TMR values should increase when incorporating Co in Fe (at least for voltages close to 0), we propose to simplify the $E(k)$ bands by considering just the bands without k dependence as sketched at the bottom in Fig. 5. One may note that, for pure Fe, (i) the majority spin $\Delta 1$ band is metallic (the Fermi level crosses the band), (ii) the minority spin $\Delta 1$ band is insulating, and (iii) both the majority- and the minority-spin $\Delta 5$ bands are metallic. This leads to some coherent tunneling current involving $\Delta 1$ and $\Delta 5$ bands in the parallel (P) configuration and only $\Delta 5$ bands in the antiparallel (AP) configuration (Fig. 5). When incorporating Co in Fe, the situation is still the same for $\Delta 1$ bands but not for $\Delta 5$ bands. Indeed, the average number of d electrons in the alloys increases, leading to an increase in the Fermi energy. The majority spin $\Delta 5$ band thus becomes insulating and there is no more conduction channel including $\Delta 5$ bulk states in the AP configuration (Fig. 5). Consequently, no coherent tunneling current takes place in the AP configuration in $Fe_{1-x}Co_x$ alloys, on the contrary to pure Fe. This explains why larger TMR values should be observed when incorporating Co in Fe.

To test this theoretical conclusion, a series of $Fe_{1-x}Co_x$/MgO-based MTJs of varying x was grown and patterned. The MgO thickness was set to 12 ML (2.5 nm) and was controlled by RHEED oscillations during the growth of each MTJ. In order to magnetically harden the top $Fe_{1-x}Co_x$ electrode and to obtain stable P and AP configurations, a thick Co layer was deposited on it at room temperature. This Co layer is relaxed in its HCP structure, for which a rather large coercive field can be reached due to the large magnetocrystalline anisotropy. The thicknesses of the top $Fe_{1-x}Co_x$ and Co layers were chosen to be equal, yielding to a coercive field around 200 Oe. Finally, a Au capping layer was used to protect the stacking. The final stacking was $Fe_{1-x}Co_x$(50 nm)/MgO (2.5 nm)/$Fe_{1-x}Co_x$(20 nm)/Co(20 nm)/Au(10 nm), with the same Co composition on both sides of the barrier. Micron-size MTJs were patterned by optical lithography and Ar ion milling. Patterned samples are 2×2 cm^2 and contain 60 MTJs with sizes ranging from 10×10 to 50×50 μm^2. The TMR was obtained by averaging the $R(H)$ curves as shown in Fig. 6(a). $I(V)$ curves were measured under a fixed magnetic field (around 50 mT for the AP configuration and 0.1 T for the P configuration) and were differentiated numerically to get the static antiparallel (G_{AP}) and parallel (G_P) conductances. Such measurements were performed at both 300 and 20 K. Figure 6 displays some of the results obtained at 20 K. As reported in a previous paper [18], and contrary to the former theoretical expectation, the TMR decreases above 25% Co, and peculiar conductance curves are obtained. For pure Fe, $G_P(V)$ is mainly parabolic, except around zero bias, where a channel opens due to the $\Delta 5$ band close to the Fermi energy [22]. This contribution at zero bias should disappear when incorporating Co, with this $\Delta 5$ band moving below the Fermi energy (see Fig. 10). However, in the range 25%–50%, a contribution around zero voltage is still observed. We show in the following that this is due to the IS observed by photoemission [18]. Finally, this G_P shape changes above 50% Co since two peaks are clearly observed around ± 0.4 V. More drastically, $G_{AP}(V)$ becomes larger than $G_P(V)$ for applied voltage higher than 0.7 V, leading to a change in the TMR sign. Apart from these drastic and clear changes in the $G_P(V)$ conductance, the $G_{AP}(V)$ curves remain surprisingly unchanged when varying the Co content. A quantitative simulation of the magnetotransport is therefore necessary to confirm the role played by the IS and by the bulk-like states of the $Fe_{1-x}Co_x$ alloys [23] in the transport process.

IV. SPIN- AND SYMMETRY-RESOLVED PHOTOEMISSION

Since photoemission is a surface sensitive technique, the samples must be prepared *in situ* in connection with the photoemission setup. This is possible on the CASSIOPEE beamline since an MBE system is connected to the spin-resolved photoemission chamber [24]. The growth process

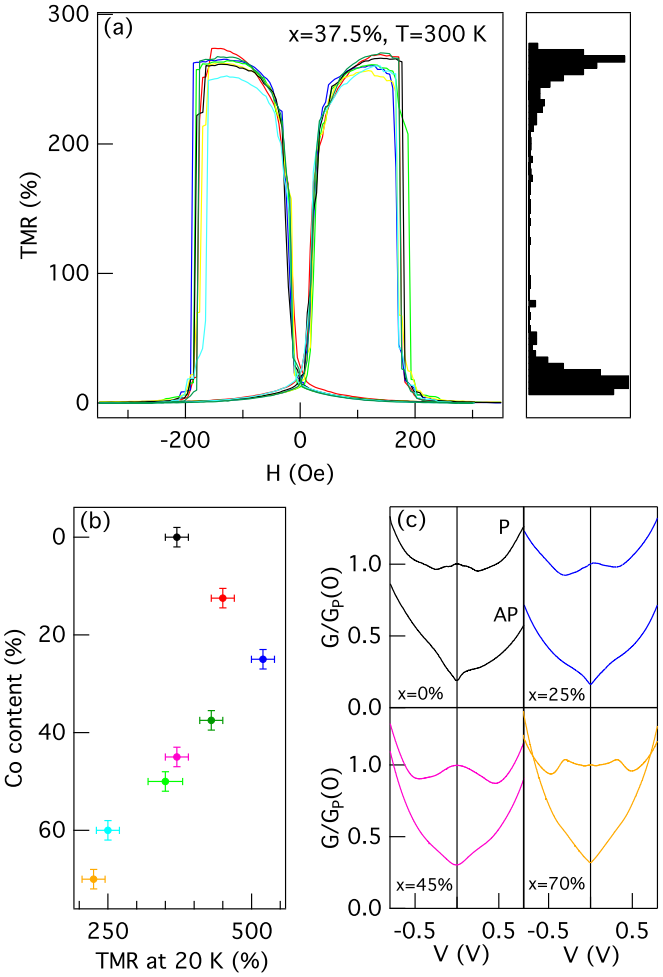

FIG. 6. (Color online) (a) Typical $R(H)$ curves measured on a series of MTJs and on the right distribution of the TMR values. (b) Variation of the TMR with Co content at 20 K. (c) Typical conductance curves for P and AP configurations at 20 K for $x = 0$, 25%, 45%, and 70%.

established in Sec. II was thus reproduced in this setup. Co and Fe were evaporated using two electron guns. The growth rates were again calibrated using RHEED intensity oscillations enabling the control of the $Fe_{1-x}Co_x$ stoichiometry with an accuracy better than $\pm 2\%$. Photoemission measurements were performed for the whole Co concentration range, with $Fe_{1-x}Co_x$ grown on Fe(001) buffer layers. In order to avoid Fe/Co intermixing, the $Fe_{1-x}Co_x$ layers were deposited on the Fe(001) buffer at room temperature without further annealing. Seven samples were prepared, with Co concentrations equal to 0, 25%, 37.5%, 5%, 62.5%, 75%, and 100%.

During spin-resolved photoemission spectroscopy (SRPES) measurements, the normal of the sample was oriented along the axis of the detector. The detector aperture corresponds to an angular integration over $\pm 1.8^\circ$ and the energy resolution was 150 meV. This geometry leads to a detection of almost only Δ states and the samples were measured in a remanent magnetized state. To eliminate instrumental asymmetry, two distinct spin-polarization measurements were performed with opposite magnetizations. As the coercive field of our films was less than 50 Oe, the applied magnetic field was set to 200 Oe to saturate the magnetization along the [100] axis prior to measurements. The spin detector is equipped with four channels, which allowed us to measure spin polarization as a function of the binding energy along the [100] (in-plane) and [001] (out-of-plane) directions. We systematically observed zero out-of-plane spin polarization, confirming that the magnetization of our films was in-plane. This also confirms that the instrumental asymmetry was fully eliminated. From the spin-polarization measurements along the [100] direction, we determined the SRPES spectra for majority and minority spin along this direction. The symmetry of the initial states involved in the transitions observed on SRPES spectra was determined by measuring successively with s or p polarizations of the incoming photons [18,26]. As the photon beam was at 45° from the normal to the sample, s-polarized photons excite only occupied $\Delta 5$ states, whereas p-polarized photons excite both occupied $\Delta 1$ and occupied $\Delta 5$ states [18,27]. To summarize, a full set of measurements on one sample consists in recording spin polarization for two opposite directions of saturating magnetic fields H, two photon polarizations ε, and three photon energies ($h\nu = 30$, 40, and

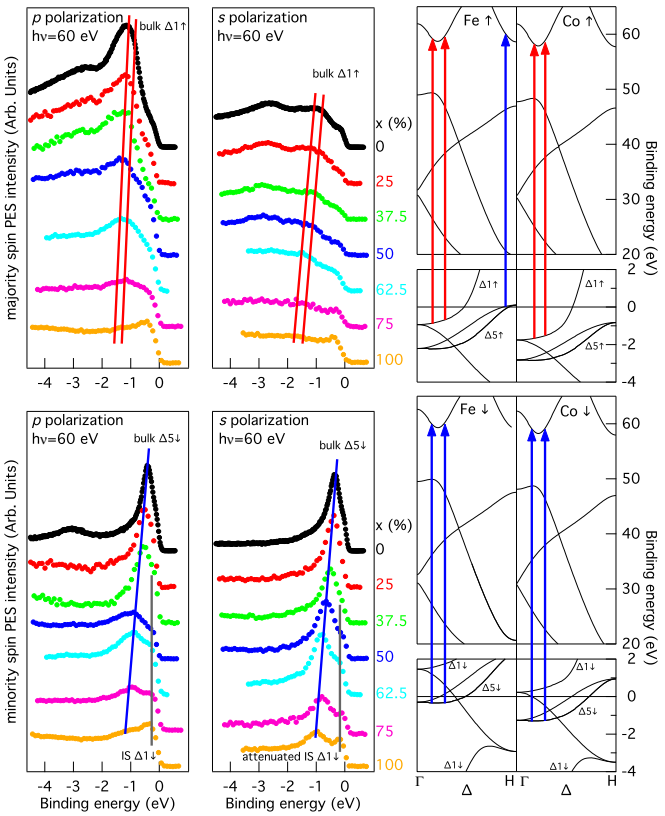

FIG. 7. (Color online) SRPES measurements using $h\nu = 60$ eV and p and s photon polarization for different Co concentrations x. The transitions ($\Delta 5 \rightarrow \Delta 1$ in blue and $\Delta 1 \rightarrow \Delta 1$ in red) coming from bulk bands were identified using band structure calculations shown here for pure Fe and pure Co (see text). The additional peak near the Fermi energy in the minority-spin channel is due to the existence of an interface state (IS). The [001] band structure was calculated with the code WIEN2K [25]; the $\Delta 1$ bands only have been represented for energies above 20 eV.

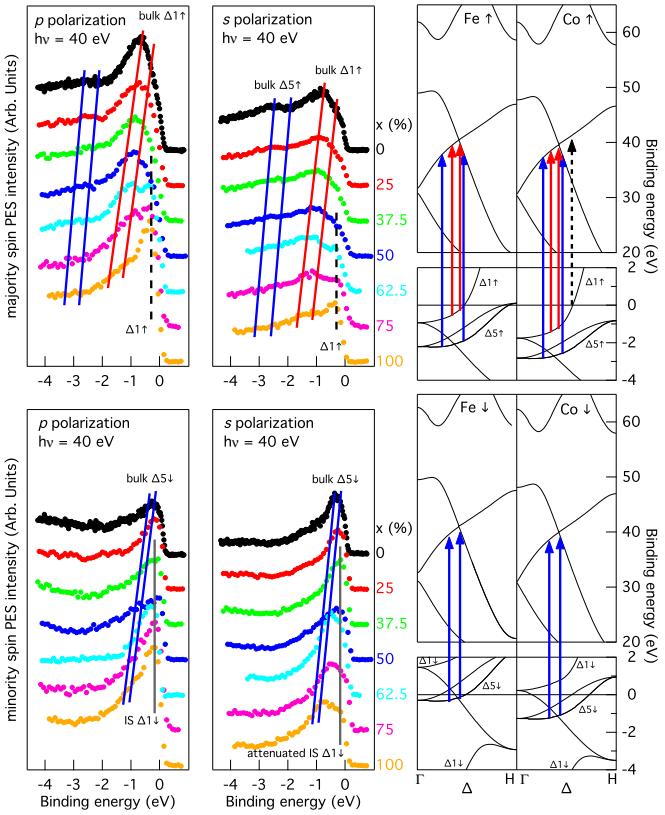

FIG. 8. (Color online) SRPES measurements and *ab initio* calculations similar to Fig. 7 using $h\nu = 40$ eV.

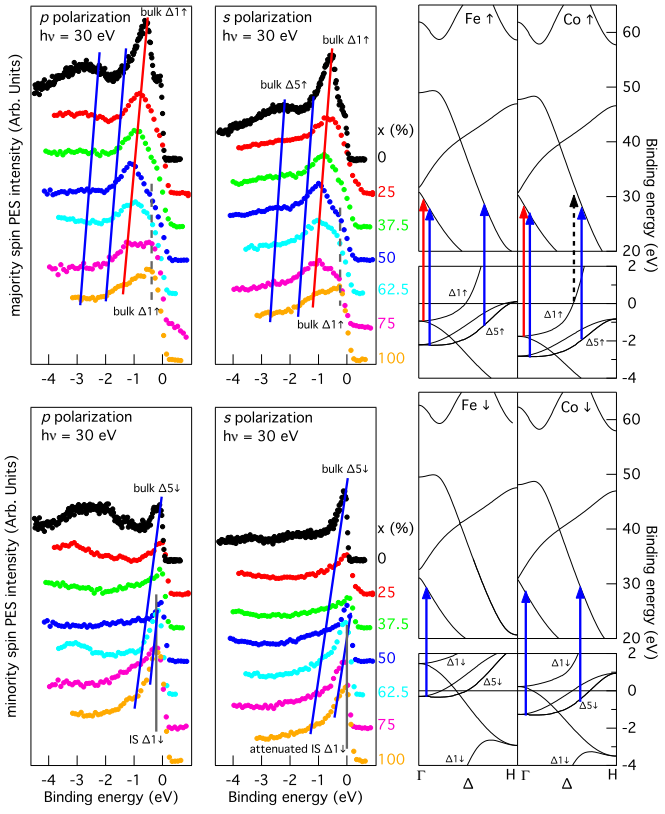

FIG. 9. (Color online) SRPES measurements and *ab initio* calculations similar to Fig. 7 using $h\nu = 30$ eV.

60 eV). The counting time was 2 h for a given set of (H, ε, $h\nu$), leading to a total counting time of 24 h for one film.

SRPES spectra obtained at three photon energies, $h\nu = 60$, 40, and 30 eV, are shown in Figs. 7, 8, and 9. Some peaks are clearly observed to be strongly attenuated when the photon polarization is switched from p to s, indicating a $\Delta 1$ symmetry of the initial states (for instance, for the spin-up channel at 40 eV in Fig. 8). In contrast, some transitions are almost unaffected when changing the photon polarization, meaning that the corresponding occupied states possess a $\Delta 5$ symmetry (for instance, for the spin-down channel at 40 eV in Fig. 8). The as-determined symmetry of the observed transitions are indicated in Figs. 7, 8, and 9. Comparison of the observed excited transitions with predicted ones using *ab initio* bulk calculations described in the following paragraph evidences an unexpected $\Delta 1$ transition observed in $Fe_{1-x}Co_x$ samples with $x > 37\%$ at a binding energy of around 0.3 eV. This state is consistent with a surface state as calculated for the free BCC Co(001) surface and was still observed when Co was covered by MgO [18]. We also verified its existence in a $Fe_{0.25}Co_{0.75}$/MgO sample [28]. In MTJs, this two-dimensional (2D) state fully spin-polarized down becomes an interfacial state, labeled IS in Figs. 7–9. These results are compared to *ab initio* calculations in the following section.

V. *AB INITIO* CALCULATIONS

To understand details of the photoemission spectra, we used the first-principles code SPRKKR [29] to calculate the Bloch spectral function along the Δ direction for disordered BCC $Fe_{1-x}Co_x$ alloys, varying x from 0 to 100% (see Fig. 10). This calculation uses the coherent potential approximation, which gives a suitable description of the chemical disorder in the $Fe_{1-x}Co_x$ alloy and allows us to go beyond the rigid band model approximation [23]. Some of the features appearing in Fig. 10 are due to the fully relativistic nature of the calculation. For pure cobalt, for instance, the degeneracy between $\Delta 1\uparrow$ states and $\Delta 5\downarrow$ states is lifted because the spin-orbit-coupling matrix elements $\langle d_{z^2}\uparrow|H_{SO}|d_{xz}\downarrow\rangle$ and $\langle d_{z^2}\uparrow|H_{SO}|d_{yz}\downarrow\rangle$ do not vanish (see the Appendix in Ref. [30]); this creates a discontinuity in the $\Delta 1\uparrow$ band. Also, the degeneracy between d_{xz} and d_{yz} $\Delta 5\uparrow$ bands is lifted because the matrix element $\langle d_{xz}\uparrow|H_{SO}|d_{yz}\uparrow\rangle$ is not equal to 0. These calculations show two important results. First, the rigid band model is a good approximation in this case. The whole band structure of Fe is unchanged when incorporating Co and the Fermi energy shifts to higher energies due to the increase in d electron number with increasing Co content. Second, some band broadening is observed for $Fe_{1-x}Co_x$ alloys due to the random distribution of Fe and Co atoms in the BCC cell. Such band broadening has to be considered in order to account for possible electronic transitions in PES.

One may go further by estimating the possible PES transitions between occupied states and empty states that fit exactly the energy of the incident photons. In order to find at which k_z and binding energy a transition is possible, we propose the following method (illustrated for a photon energy equal to 40 eV; Fig. 11). The energy diagram of the empty states is superimposed on the energy diagram of the occupied states by aligning the 40-eV energy to the Fermi

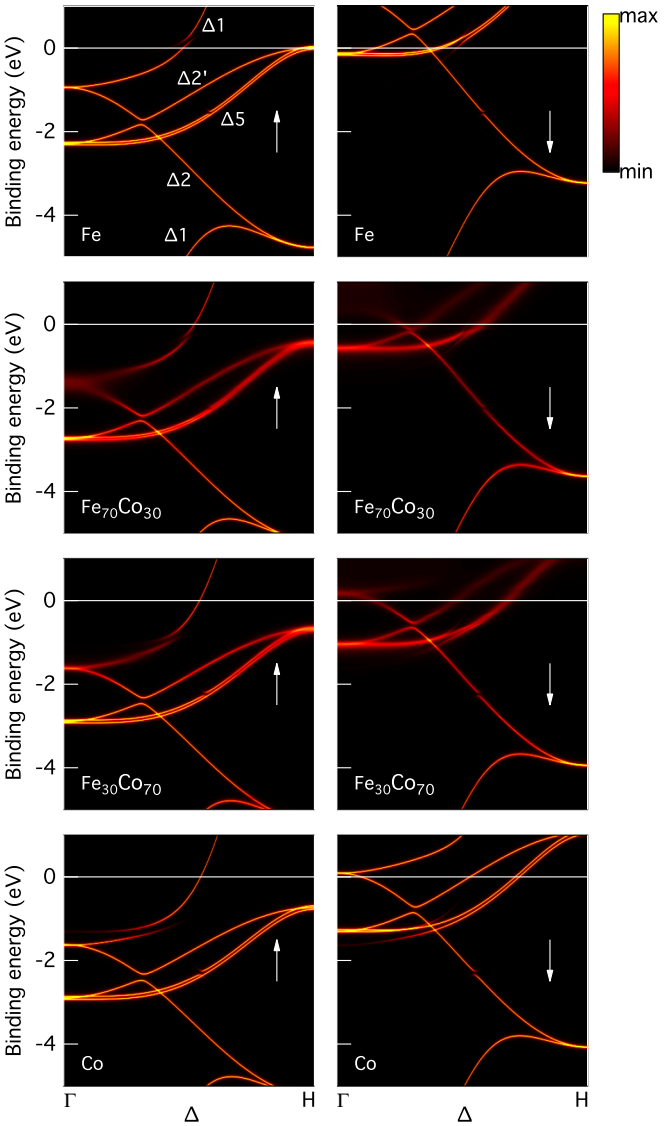

FIG. 10. (Color online) Bloch spectral function calculated with the code SPRKKR along Γ-H for bulk BCC $Fe_{1-x}Co_x$, for $x = 0$, 0.3, 0.7, and 1, for both majority spin (left) and minority spin (right).

level. Each intersection between the final empty states and the initial occupied states correspond to a 40-eV separation at a fixed k_z [27,31]. The corresponding transitions are thus systematically determined for pure Fe and Co and compared to experimental transitions in Figs. 7–9. As the rigid band model is a good approximation to describe the band shift when incorporating Co in Fe, a linear displacement of the transition energy from pure Fe to pure Co is assumed.

The general agreement between simulated and experimental transitions is very good. The observed spectra obtained for pure Fe and Co are also in agreement with reported results [27,31]. As expected, the Δ1 occupied states are excited for the three photon energies using p polarization and attenuated using s polarization. For $h\nu = 60$ eV, the Δ1 and Δ5 PES transitions are well reproduced by bulk band calculations for the whole Co concentration. In addition to these transitions coming from the bulk states, the minority-spin surface state is observed for a Co concentration above 37%.

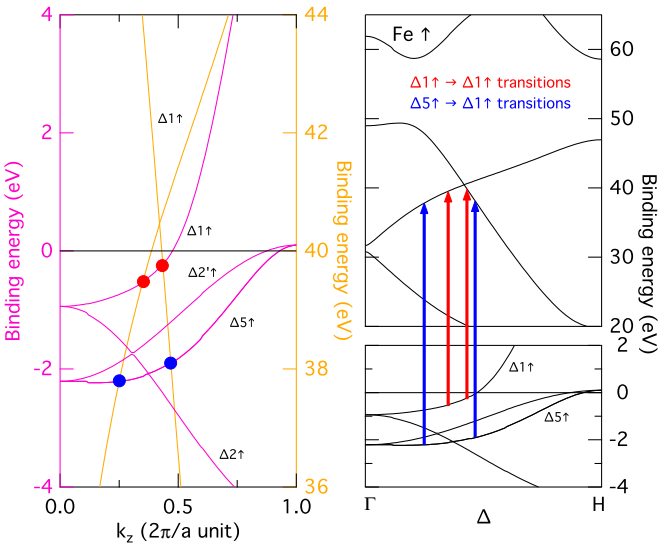

FIG. 11. (Color online) Method to obtain the possible electronic transitions here for a 40 eV photon energy. Left: The occupied states energy diagram is superimposed on the empty states energy diagram by superimposing the Fermi level to the 40-eV energy. Right: Each intersection between occupied and empty bands gives a transition separated by exactly 40 eV. These obtained transitions are thus plotted on the band structure.

For $h\nu = 40$ eV, the situation is very similar except that an additional transition is observed at a binding energy of around −0.5 eV in the majority-spin channel for a Co concentration above 50%. This transition is not expected from calculations if we consider sharp and well defined bulk bands as in Fig. 11. However, the random chemical disorder between Fe and Co in the BCC crystal induced some broadening of the bands. This band broadening enables a new transition coming from the Δ1 majority band in the middle of the Brillouin zone close to the Fermi energy as indicated by the dashed arrow in Fig. 8. Since the Fermi energy increases with increasing Co content, this transition is not possible for pure Fe but becomes possible for a Co concentration above 50%. For $h\nu = 30$ eV, this additional transition is also observed (dashed arrow in Fig. 10). The general analysis of the PES spectra is, however, trickier for this 30-eV photon energy. First, two transitions involving majority-spin Δ1 and Δ5 bands are found to be close in energy (around −1 eV binding energy). The band symmetry resolution using p- and s-photon polarizations is thus not obvious in this particular case. Moreover, a new minority-spin Δ5 transition near the Fermi energy is simulated for a Co content above 50% and superimposed on the minority-spin surface state. Again, distinguishing this minority-spin Δ5 bulk state and minority-spin Δ1 surface state is not obvious, even if a clear Δ1 contribution is evidenced experimentally, since the intensity is strongly reduced using s polarization.

Finally, our analysis in terms of bulk-like states and IS should allow us to understand the peculiar conductance curves in Fig. 6. One should note that two new contributions in the conductance have to be taken into account [18]. First, the spin-down Δ1 IS certainly impacts the conductance since it offers a new Δ1 conduction channel in the AP configuration from bulk-like Δ1↑ states to the Δ1↓ IS. But this is not

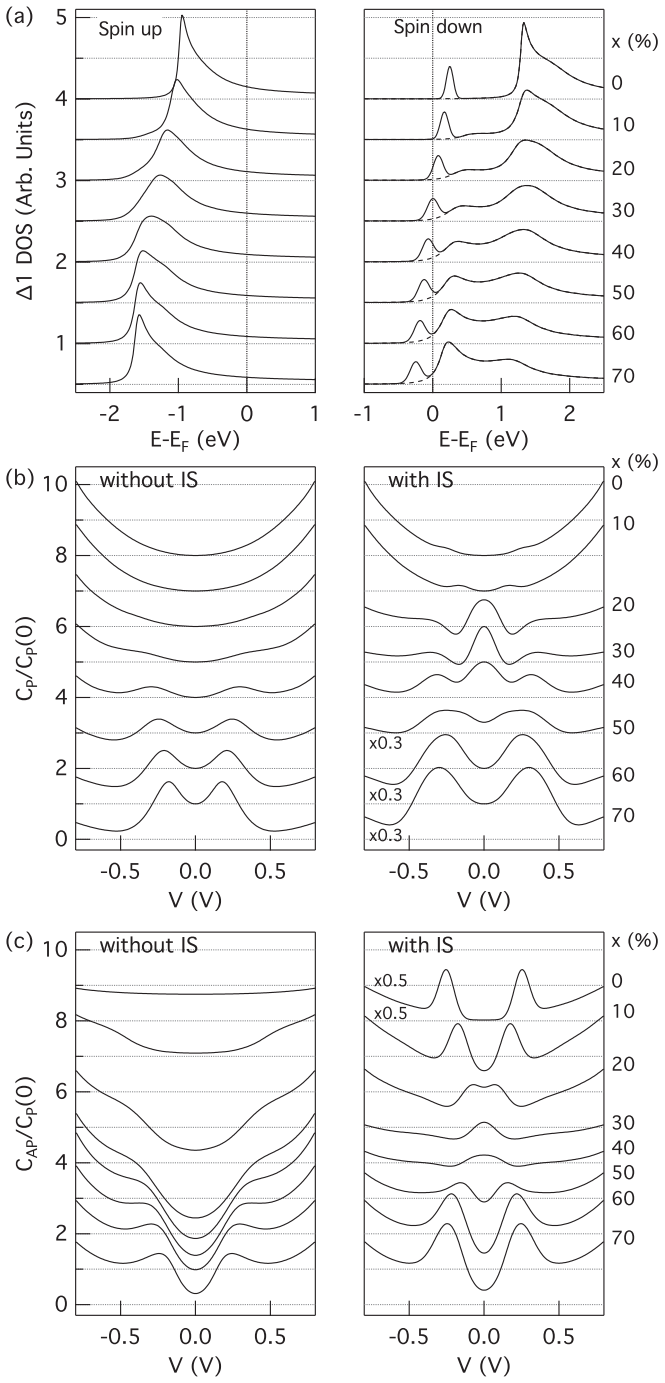

FIG. 12. (a) Δ1 DOS used to estimate the parallel conductance, for several values of the Co content, with (solid curves) and without (dashed curve) the contribution of the IS represented by a Gaussian function. (b) Parallel conductance estimated from the self-convolution of the Δ1 DOS without (left) and with (right) the contribution of the IS. (c) The same, for the antiparallel conductance.

the only contribution. The first-principles calculations indeed suggest that, because of alloy disorder, the edge of the $\Delta 1\downarrow$ bulk-like band (which is empty for the whole Co concentration range) crosses the Fermi level above 30% Co [the tail of the corresponding density-of-states (DOS) curve becomes broadened, as shown in Fig. 12(a)]. Additional conduction channels including this contribution thus have to be taken into account to explain the conductance curves. These additional conduction channels should intuitively have a large impact on both P and AP conductance with increasing Co content, while strong modifications in P conductance were observed, although the AP conductance seemed not to be so much affected (Fig. 6). We performed a rough estimation of the contribution of Δ1 electron states to the conductance $G_P(V) = \mathrm{d}I_P(V)/\mathrm{d}V$ in the P configuration by calculating and differentiating with respect to V the expression

$$\sum_{\sigma=\uparrow,\downarrow} \int_{E_F-eV}^{E_F} \rho_{\Delta 1,\sigma}(E)\rho_{\Delta 1,\sigma}(E+eV)dE,$$

where $\rho_{\Delta 1,\uparrow}(E)$ and $\rho_{\Delta 1,\downarrow}(E)$ are the density of the$\Delta 1\uparrow$ and $\Delta 1\downarrow$ states represented in Fig. 12(a). A similar calculation using the appropriate DOS is also performed for AP configuration. These DOSs correspond to the sum of the bulk Δ1-DOS calculated with the code SPRKKR and of a model Gaussian function crossing the Fermi level when the Co content increases, which corresponds to the contribution of the $\Delta 1\downarrow$ IS. It should be noted that the barrier transmission is not included here, so these calculated values are called $C_P(V)$ and $C_{AP}(V)$ in the following. Figure 12 shows the contribution of Δ1 states to the P [Fig. 12(b)] and AP [Fig. 12(c)] conductances calculated from this rough estimation of the tunnel current, where bulk-like states and IS are both taken into account (right-side curves) and with bulk-like states only (left-side curves). Looking first at the P configuration curves, they show that the maximum of the P conductance observed at low voltage for the Co content in the range 25%–50% can be attributed to a clear IS contribution, while the maximum of the P conductance measured for Co-rich alloys around 0.3 V is due to the minority-spin IS and bulk-like states which cross the Fermi level due to the alloy-induced broadening of the $\Delta 1\downarrow$ band edge. Despite its rough character (Δ1 DOS only, simple model function for the IS contribution, forgetting the scattering properties of the MgO barrier), this simple estimation of the tunnel current succeeds in explaining the physical origin of the surprising features observed in P conductance. The situation is not as clear concerning AP conductance. If the calculated C_{AP} curves that do not consider the IS contribution are not so far from the measurements in Fig. 6, this is not the case when the IS state is taken into account. In particular, a clear contribution of the empty IS is obtained for C_{AP} for pure Fe/MgO/Fe, although such a large IS footprint has not been observed either in our samples or in the literature. One possible explanation is that the coupling between the IS state and the bulk states (leading to a so-called interface resonant state) is not strong, leading to an attenuated footprint in the AP conductance curves. It should also be noted that the calculated TMR values in these Fe/MgO or Co/MgO MTJs is much larger than the experimental ones. This means that other conduction channels occur, for instance, due to some mixing of the symmetry or spin-flip due to defects at the interfaces or in the MgO barrier. The impact of such scattering on defects should be much more important for AP conductance since the AP coherent tunneling (with spin and symmetry conservation) considering only the bulk states in BCC $Fe_{1-x}Co_x$ alloys is equal to 0 (for zero voltage) as shown in Fig. 6. Thus any scattering events even with low probabilities

should especially impact AP conductance. More sophisticated first-principles investigations have been performed recently to calculate the P conduction in $Fe_{1-x}Co_x$ MTJs, but these calculations do not reproduce the voltage-dependent features of the P conductance observed in experiments [32].

VI. CONCLUSION

In summary, good control of the structure and stoichiometry of $Fe_{1-x}Co_x(001)$ epitaxial layers was achieved with the help of electron diffraction, XPS, and Auger spectroscopy. Moreover, we show that the low Fe/Co intermixing temperature (250°C) may explain some controversial results in the literature. The MgO-based MTJs built with such magnetic electrodes have very peculiar TMR and conductance curves that are explained here using both spin- and symmetry-resolved photoemission analysis and *ab initio* calculations. The bulk band structure calculations, but also the existence of a 2D $\Delta 1$ state in these chemically disordered BCC $Fe_{1-x}Co_x(001)$ epitaxial layers, match very well with electronic transitions observed by photoemission. This general analysis of PES spectra with the help of *ab initio* calculation also shows that the choice of photon energy excitation to perform symmetry-resolved photoemission is crucial. If the transition analysis is easy using 60 eV photon energy, the situation is trickier using 30 eV due to the occurrence of both $\Delta 1$ and $\Delta 5$ transitions at similar binding energies. The band broadening due to the chemical disorder between Fe and Co within the BCC crystal also allows some additional transitions. Finally, the peculiar conductance curves are qualitatively well explained taking into account both the IS state and the bulk $\Delta 1\downarrow$ states, except for the too large contribution of the IS state in simulated AP conductance compared to experiments. This discrepancy may be explained by symmetry mixing that is particularly efficient at a surface or interface, which may destroy the resonance. To conclude, both bulk bands and IS contributions are thus at the origin of the TMR decrease observed above 25% Co in FeCo-MgO(001) MTJs grown by MBE.

ACKNOWLEDGMENTS

The calculations presented in this article were performed at the CALMIP/UPS Toulouse parallel computer center. The authors from IJL want to acknowledge the Région Lorraine for its financial support.

[1] W. H. Butler, X.-G. Zhang, T. C. Schulthess, and J. M. MacLaren, Phys. Rev. B **63**, 054416 (2001).
[2] J. Mathon and A. Umerski, Phys. Rev. B **63**, 220403 (2001).
[3] X.-G. Zhang and W. H. Butler, Phys. Rev. B **70**, 172407 (2004).
[4] S. Yuasa, T. Nagahama, A. Fukushima, Y. Suzuki, and K. Ando, Nat. Mater. **3**, 868 (2004).
[5] S. S. P. Parkin, C. Kaiser, A. Panchula, P. M. Rice, B. Hughes, M. Samant, and S.-H. Yang, Nat. Mater. **3**, 862 (2004).
[6] C. Tiusan, M. Sicot, J. Faure-Vincent, M. Hehn, C. Bellouard, F. Montaigne, S. Andrieu, and A. Schuhl, J. Phys.: Condens. Matter **18**, 941 (2006).
[7] M. Sicot, S. Andrieu, P. Turban, Y. Fagot-Revurat, H. Cercellier, A. Tagliaferri, C. De Nadai, N. B. Brookes, F. Bertran, and F. Fortuna, Phys. Rev. B **68**, 184406 (2003).
[8] V. Serin, S. Andrieu, R. Serra, F. Bonell, C. Tiusan, L. Calmels, M. Varela, S. J. Pennycook, E. Snoeck, M. Walls, and C. Colliex, Phys. Rev. B **79**, 144413 (2009).
[9] X.-G. Zhang, W. H. Butler, and A. Bandyopadhyay, Phys. Rev. B **68**, 092402 (2003).
[10] B. D. Yu and J.-S. Kim, Phys. Rev. B **73**, 125408 (2006).
[11] F. Bonell, S. Andrieu, A. M. Bataille, C. Tiusan, and G. Lengaigne, Phys. Rev. B **79**, 224405 (2009).
[12] J. P. Velev, K. D. Belashchenko, S. S. Jaswal, and E. Y. Tsymbal, Appl. Phys. Lett. **90**, 072502 (2007).
[13] G. X. Miao, Y. J. Park, J. S. Moodera, M. Seibt, G. Eilers, and M. Münzenberg, Phys. Rev. Lett. **100**, 246803 (2008).
[14] F. Bonell, S. Andrieu, C. Tiusan, F. Montaigne, E. Snoeck, B. Belhadji, L. Calmels, F. Bertran, P. Le Fèvre, and A. Taleb-Ibrahimi, Phys. Rev. B **82**, 092405 (2010).
[15] S. Yuasa, T. Katayama, T. Nagahama, A. Fukushima, H. Kubota, Y. Suzuki, and K. Ando, Appl. Phys. Lett. **87**, 222508 (2005).
[16] S. Yuasa, A. Fukushima, H. Kubota, Y. Suzuki, and K. Ando, Appl. Phys. Lett. **89**, 042505 (2006).
[17] Y. M. Lee, J. Hayakawa, S. Ikeda, F. Matsukura, and H. Ohno, Appl. Phys. Lett. **90**, 212507 (2007).
[18] F. Bonell, T. Hauet, S. Andrieu, F. Bertran, P. Le Fèvre, L. Calmels, A. Tejeda, F. Montaigne, B. Warot-Fonrose, B. Belhadji, A. Nicolaou, and A. Taleb-Ibrahimi, Phys. Rev. Lett. **108**, 176602 (2012).
[19] See, for instance, G. Ertl and J. Küppers, *Low Energy Electrons and Surface Chemistry* (Wiley-VCH Verlag, Weinheim, 1986).
[20] J. Dekoster, E. Jedryka, C. Mény, and G. Langouche, Europhys. Lett. **22**, 433 (1993).
[21] See, for instance, I. V. Markov, *Crystal Growth for Beginners: Fundamentals of Nucleation, Crystal Growth, and Epitaxy* (World Scientific, Singapore, 1995).
[22] F. Greullet, C. Tiusan, F. Montaigne, M. Hehn, D. Halley, O. Bengone, M. Bowen, and W. Weber, Phys. Rev. Lett. **99**, 187202 (2007).
[23] B. Belhadji and L. Calmels, Phys. Rev. B **83**, 092401 (2011).
[24] For details see http://www.synchrotron-soleil.fr/Recherche/LignesLumiere/CASSIOPEE.
[25] P. Blaha, K. Schwarz, G. K. H. Madsen, D. Kvasnicka, and J. Luits, *WIEN2k, An Augmented Plane Wave + Local Orbitals Program for Calculationg Crystal Properties* (Karlheinz Schwarz Techn. Universität Wien, Austria, 2001); http://www.wien2k.at.
[26] P. D. Johnson, Rep. Prog. Phys. **60**, 1217 (1997).
[27] L.-N. Tong, F. Matthes, M. Müller, C. M. Schneider, and C.-G. Lee, Phys. Rev. B **77**, 064421 (2008).

[28] S. Andrieu, F. Bonell, T. Hauet, F. Montaigne, L. Calmels, E. Snoeck, P. Le Fèvre, and F. Bertran, J. Appl. Phys. **115**, 172610 (2014).

[29] H. Ebert *et al.*, The Munich SPRKKR package, version 3.6 (http://olymp.cup.uni-muenchen.de/ak/ebert/SPRKKR); H. Ebert, Lect. Notes Phys. **535**, 191 (2000).

[30] F. Gimbert and L. Calmels, Phys. Rev. B **86**, 184407 (2012).

[31] L.-N. Tong, C.-L. Deng, F. Matthes, M. Müller, C. M. Schneider, and C.-G. Lee, Phys. Rev. B **73**, 214401 (2006).

[32] C. Franz, M. Czerner, and C. Heiliger, Phys. Rev. B **88**, 094421 (2013).